Journal of Petroleum Science and Engineering 208 (2022) 109606

Contents lists available at ScienceDirect

Journal of Petroleum Science and Engineering

journal homepage: www.elsevier.com/locate/petrol

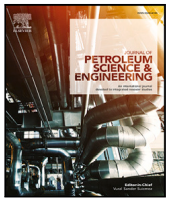

Effects of methane hydrates on two-phase relative permeability in sandstone: Numerical simulation of laboratory experiments

Alejandro Bello-Palacios [a,b,*], Per Fotland [a], Stian Almenningen [b], Geir Ersland [b]

[a] Equinor ASA, Bergen, Norway
[b] Department of Physics and Technology, University of Bergen, Norway

ARTICLE INFO

Keywords:
2-phase flow
Clathrates
TOUGH+HYDRATE
Verification

ABSTRACT

To identify the challenges and limitations in measuring and modelling gas relative permeability in hydrate bearing sandstone, we simulate a series of experiments. Experimental and numerical results are used to examine the amount of hydrates formed as well as how the flow of gas is affected by the hydrate formation. The reservoir simulator TOUGH+HYDRATE was used. The system is represented numerically in both 1-dimensional and 2-dimensional grids. The 1-dimensional simulations are used to check the system consistency by keeping track of the amount of hydrates that are formed, given the initial and boundary conditions. The 2-dimensional simulations are used to measure the effects of heterogeneity in the distribution of hydrates, and its impact on both relative permeability and capillary pressure. The results reveal complexities when comparing experimental and simulated permeability in hydrate-bearing systems. The results from the 1-dimensional calculations show that most experiments have not been able to form the amount of hydrates that is theoretically possible by the initial mix of brine and gas. This indicates that early growth of hydrates can limit mass transfer to inner parts of the core shielding the system for further nucleation. This is supported by the 2-dimensional simulations. These show how a heterogeneous pattern of hydrates can limit fluid flow by (a) reducing the intrinsic permeability, (b) scaling down gas relative permeability, and (c) and scaling up capillary entry pressure of portions of the core. Although these effects do not fully explain the experimental results, the results provide insight to hydrate induced flow restrictions and how these can affect experimental result.

1. Introduction

Gas hydrates are crystalline ice-like solids formed by the mixing of water and a gas under pressure. Water molecules form hydrogen-bonded structures with cavities that are stabilized by the filling of non-polar or slightly polar guest gas molecules (Sloan et al., 2007). Methane is the most common gas molecule that forms hydrates naturally. Besides the availability of both water and methane, low temperatures and high pressures are needed. Porous media in and below permafrost and near seafloor sediments in deep marine regions (water column higher than 400 m) meet these conditions and host most methane hydrate accumulations known in the world (Boswell, 2009). These accumulations have gained increased interest over the last four decades and multiple research initiatives are focusing on understanding their impact on safety in drilling operations, seafloor stability, climate change, geohazards, and its feasibility as a potential energy resource (Collett et al., 2014).

Natural or human induced changes in pressure and temperature will affect the stability of hydrates and may cause formation of hydrates or melting and reformation. This involves a dynamic transition between a system with 2 phase flow (gas and water) and 1 solid phase (hydrates).

Depending on whether the hydrates form or melt in a saline environment a number of changes take place; 1. heat is either consumed or released causing a temperature change 2. pressure may decrease or increase due to both gas and water consumption or release, 3. the salinity decreases or increases as water is consumed or released. All these mechanisms may have significant impact on the hydrate distribution and flow of fluids. To complicate matters even more there is an apparent stochastic nature to hydrate formation. Once hydrate nuclei are formed, they will consume nearby gas and water and grow until the driving forces are locally zero, due to lack of methane, water or an increased salinity. This may cause the overall formation to become patchy (Fig. 1). If in addition the porous medium is un-consolidated, the internal hydrate pressure of the small nuclei may be higher than the surrounding effective pressure and thereby grains can be moved and the patch may grow to become a single solid hydrate lens or vein (Jang and Santamarina, 2016).

In multi-phase flow, the saturation of each phase determines how it flows and inhibits the flow of the coexisting phases. This effect is

* Corresponding author.
E-mail address: gpb@equinor.com (A. Bello-Palacios).

https://doi.org/10.1016/j.petrol.2021.109606
Received 12 October 2020; Received in revised form 13 April 2021; Accepted 4 October 2021
Available online 12 October 2021
0920-4105/© 2021 The Author(s). Published by Elsevier B.V. This is an open access article under the CC BY license (http://creativecommons.org/licenses/by/4.0/).

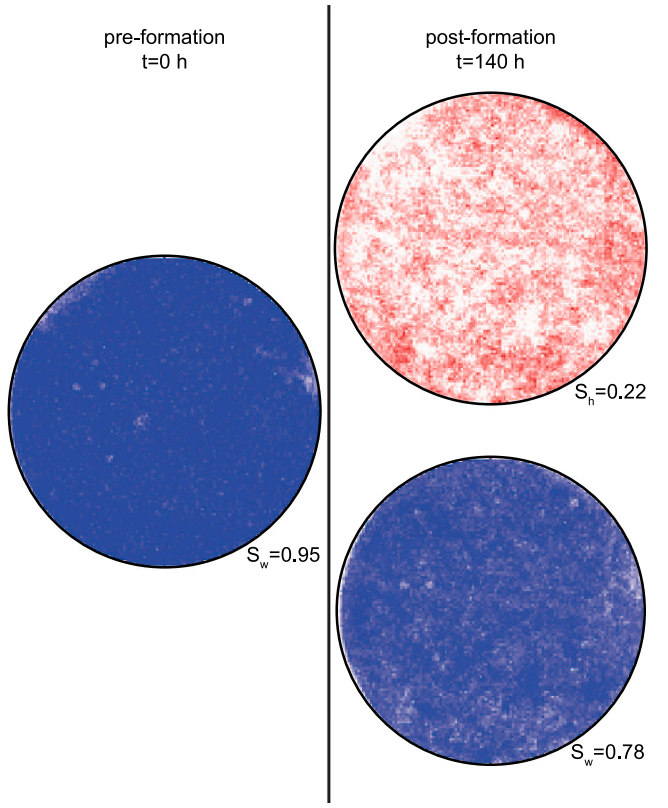

Fig. 1. MRI images of a cross-sectional slice of a Bentheim sandstone core. Images display phase saturations before (left) and after (right) hydrate formation. Post-formation phase saturation is resolved for both hydrates (red) and brine (blue). Hydrate saturation (top right) shows a heterogeneous stochastic (“patchy”) pattern.

described by the phase relative permeability. Reliable relative permeability estimates are central to the accuracy of numerical predictions of flow in porous media (Kleinberg et al., 2003).

In terms of laboratory experiments, the most common technique for permeability measurements is the steady state flow test (Li et al., 2018). The complexities of multi-phase flow in hydrate bearing systems makes the measurement of relative permeability particularly difficult. Every phase affects each other while the intrinsic permeability of the medium actively changes. In addition, though pressure and temperature must be maintained during tests, it is very hard to avoid hydrate re-formation and dissociation (Moridis et al., 2010). The number of studies published is low (Jaiswal, 2004; Ahn et al., 2005; Johnson et al., 2011; Almenningen et al., 2019) and include a variety of methods and materials. Ren et al. (2020) concludes that the variability between these studies reveals a lack of repeatability and a challenge of making their results comparable.

Almenningen et al. (2019) published a series of measurements of gas relative permeability in carbon dioxide (CO_2) and methane (CH_4) hydrate bearing sandstone. The experiment setup considered varying saturations of both gas and brine, expecting to measure the effect of the presence of both hydrates and the fluid phases. Results show a clear but highly scattered decreasing trend of gas permeability with increasing hydrate saturation. It is suggested that this effect can be related to methane becoming disconnected by hydrate films that form local barriers of flow and that the distribution of such flow barriers vary between experiments.

In terms of combining experimental studies on hydrate bearing porous media with numerical models, there has been relatively few studies. Jang and Santamarina (2014) used numerical modelling to reproduce permeability and capillary pressure relationships monitored through hydrates in micromodels. Chen et al. (2018), used numerical models to calculate gas relative permeability as a function of hydrate distribution obtained from X-ray microtomography images from hydrate bearing sandpacks.

To estimate bulk phase saturations in laboratory measurements involving hydrate formation or dissociation of porous media, exchange of fluids along with pressure and temperature are monitored. However, in the absence of tools that provide images that can distinguish solid hydrates from fluid phases, it is impossible to see how these phases are distributed internally.

Numerical modelling can assist the analysis of experimental measurements where the internal distribution of phases could have been critical in the quality of the physical measurement. Modelling can be critical to complement the work done in the laboratory and enable extrapolation of laboratory measurements to field-scale applications. Similarly, experimental results can assist constraining the models that define how the internal porous media is affected by the presence of hydrates. A good agreement between experimental data and numerical predictions is essential to bridge knowledge gaps and improve understanding of the complexity of gas hydrates systems (Birkedal et al., 2014).

To address this issue, we present the results of simulating 2-phase flow effective permeability experiments from Almenningen et al. (2019)) using TOUGH+HYDRATE (T+H).

- Firstly, we compare how suitable T+H is to reproduce the process of hydrate formation after cooling down pressurized gas and brine.
- Secondly, we evaluate how T+H can help to understand processes that were not possible to observe during the experimental work. Particularly on the internal distribution of both solid and fluid phases on the effective gas flow. This includes how a stochastic hydrate growth affects both capillary pressure and intrinsic permeability.
- Finally, with the results obtained in this work we aim to map out potential caveats and limitations that can be encountered when designing experiments that involve hydrates in porous media.

2. Methods

The dataset used for this work consists of end-point gas relative permeability measurements in sandstone, before and after hydrate formation (Almenningen et al., 2019) (Table 1). A set of cylindrical sandstone cores initially saturated with methane gas and brine (3.5 wt% NaCl) were connected to flowlines on each end of the core to provide the necessary influx to pressurize the core and measure relative permeability. A cooling jacket was used to cool down the core and induce the formation of hydrates at constant pressure.

Each experiment produced a relative permeability measurement before and after hydrate formation (Fig. 2). Hydrate saturation achieved after cooling was between 37% and 61%. The relative permeability due to hydrate formation was decreased by 1 to 5 orders of magnitude.

To model these results, TOUGH+HYDRATE v1.5 (T+H) was used. T+H is a numerical code for the simulation of the behaviour of methane hydrate-bearing geologic systems for multi-phase, multi-component flow and transport of mass and heat through porous and fractured media (Moridis and Pruess, 2014).

Hydrate formation and dissociation are modelled in T+H by using either an equilibrium or a kinetic model. In the equilibrium model, phase transitions are governed only by pressure and temperature. Water and methane are mass components, and hydrate is one of the potential phases that can be present in different combinations (Fig. 3). In the kinetic model, hydrates are treated as a new mass component. Phase transitions are calculated by kinetic parameters in an Arrhenius-type expression based on the work of Kim et al. (1987). Eq. (1) describes the behaviour of the hydrate mass component and phase.

$$\frac{\partial M}{\partial t} = K_0 e^{(-\Delta E_a/RT)} F_A \; A_S \; (f_{eq} - f_v) \tag{1}$$

Table 1
List of all CH_4 permeability experiments (Almenningen et al., 2019). Core pressure and temperature were kept constant at 8.3 MPa and 4 °C, respectively, during hydrate formation and permeability measurements. Margin of errors reflect instrumental uncertainties. (For interpretation of the references to colour in this figure legend, the reader is referred to the web version of this article.)

Exp. ID	No hydrate		Hydrate		
	S_g [frac.] ±0.01	k_{rg} [frac.]	S_{hyd} [frac.] ±0.02	S_g [frac.] ±0.02	k_{rg} [frac.]
A	0.54	0.12 ± 0.02	0.46	0.44	1.9E−2 ± 0.3E−2
B	0.47	0.19 ± 0.08	0.47	0.36	1.2E−3 ± 0.4E−3
C	0.46	0.09 ± 0.03	0.45	0.36	1.7E−6 ± 0.6E−6
D	0.46	0.06 ± 0.02	0.47	0.36	4E-6 ± 1E−6
E	0.46	0.06 ± 0.02	0.51	0.35	1.4E−4 ± 0.5E−4
F	0.36	0.08 ± 0.03	0.61	0.23	4E-7 ± 1E−7
G	0.36	0.14 ± 0.02	0.53	0.24	9.9E−7 ± 0.8E−7
H	0.27	0.032 ± 0.006	0.37	0.18	7.1E−7 ± 0.8E−7

S_g and S_{hyd} are the gas and methane saturations, respectively; k_{rg} is the relative permeability of gas.

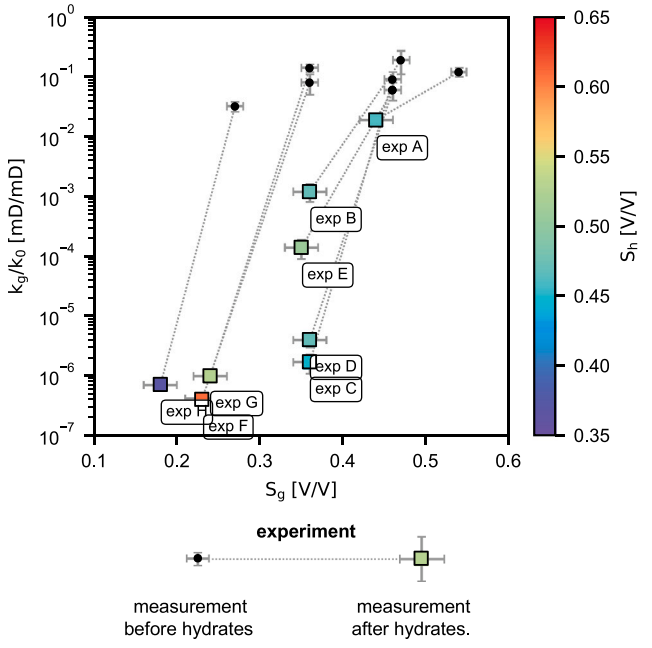

Fig. 2. Overview of all the methane relative permeability measurements and margin of errors. Black circles show gas relative permeability before hydrate formation. Coloured squares show relative permeability after hydrate formation. Colour shade in squares represents hydrate saturation. Stippled lines connect measurements in each experiment. (For interpretation of the references to colour in this figure legend, the reader is referred to the web version of this article.)

Where $^{\partial M}/_{\partial t}$ is the methane mass rate, K_0 the intrinsic hydration reaction constant, ΔE_a the hydration activation energy, R is the universal gas constant, T is the temperature, F_A is the area adjustment factor, A_S is the hydrate reactive surface area, f_{eq} is the fugacity at equilibrium temperature and f_v is the fugacity in the gas phase at temperature T.

Kowalsky and Moridis (2007), Teng and Zhang (2020) have compared both modelling strategies. Kowalsky and Moridis (2007) concluded that they were practically indistinguishable for large-scale and long-term processes, but that Kinetic model would more suitable for short-term and core-scale simulations. Teng and Zhang (2020) conclude that the equilibrium model is a special case of kinetic model where the relative strength of the hydrate reaction is greater than that of other physical processes. The authors also indicate that when such strength is relatively smaller than other physical processes, the kinetic model can be more computationally efficient. Birkedal et al. (2014) observed that the kinetic model was less sensitive to temperature variations at the boundary condition and was more numerically efficient.

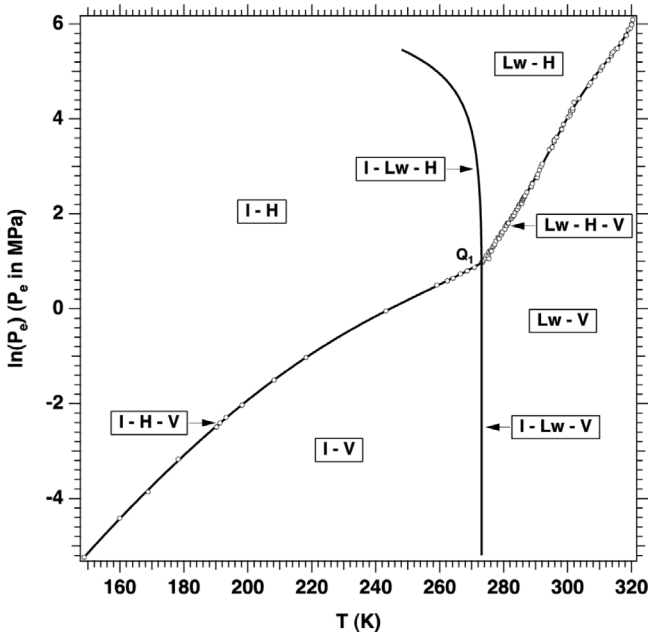

Fig. 3. Pressure–temperature equilibrium relationship in the phase diagram of the water–methane–hydrate system. All possible combinations of the four phases are displayed: aqueous (Lw), ice (I), gas (V), and hydrate (H) (Moridis and Pruess, 2014).

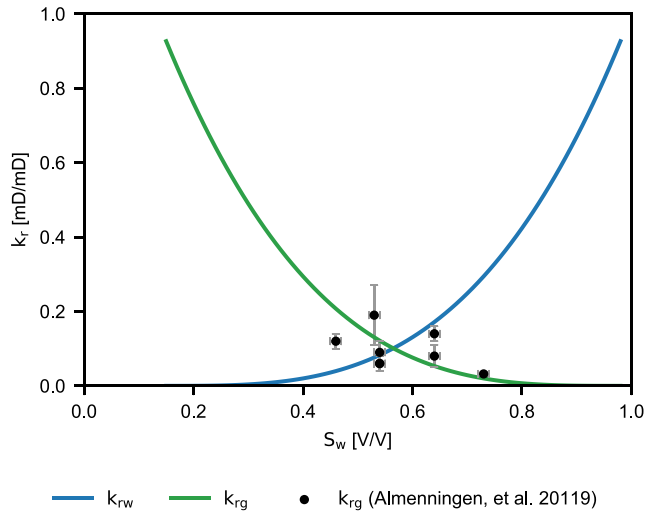

Fig. 4. 2-phase relative permeability curves used in this study based on the modified Stone model. k_w, k_r are water and gas relative permeability, respectively. Overlaid, 2-phase gas relative permeability measurements, prior to hydrate formation (Almenningen et al., 2019).

Water and gas flow in hydrate bearing rocks is governed by fluid saturations and the reduction in porosity due to hydrate formation. T+H handles this by using separate models that define two-phase relative permeability and growth of solid (hydrate). For relative permeability, the modified Stone model was used in T+H. It is a power-law relationship between the relative permeability of the fluid phase (k_{rw}, k_{rg}) and the saturation of the phase (S_w, S_g) (Fig. 4), defined by Eqs. (2) and (3).

$$k_{rw} = \frac{k_w}{k_0} = \left(\frac{S_w - S_{rw}}{1 - S_{rw}}\right)^{n_w} \tag{2}$$

$$k_{rg} = \frac{k_g}{k_0} = \left(\frac{S_g - S_{rg}}{1 - S_{rw}}\right)^{n_g} \tag{3}$$

Table 2
TOUGH+H input parameters used for sandstone cores.

Parameter	Magnitude
Porosity [V/V]	$\phi_0 = 0.22$
Absolute permeability [D]	$k_0 = 1.3$–1.9
Initial salinity [wt.%]	$X_{inh} = 3.5$[a]–5.44[b]
Model for updating porosity and permeability	$m = 3$[a]
	$\phi_c = 0.05$[a]
Relative permeability. Modified Stone model	$S_{ira} = 0.15$, $S_{irg} = 0.05$[a]
	$n_a = 3.5$, $n_g = 3.2$[a]

[a]Values taken from Birkedal et al. (2014).
[b]Arbitrarily defined value to estimate highest reduction of permeability.

S_{rw} and S_{rg} are residual saturation of water and gas phases, respectively. Both these parameters and fitting exponents n_w, n_g define the shape and end-points of the curves (Fig. 2) and are to be defined by the user. The small amount of experiments yielded a scattered amount of relative permeability measurements (Fig. 2). There is no unique solution for the Stone model. Therefore, residual saturations and fitting exponents for both gas and water were taken from Birkedal et al. (2014) (Table 1).

The solid hydrate phase in T+H is modelled as an extension of the matrix. Effective or (hydrate-filled) porosity (ϕ) is a function of both the initial (hydrate-free) porosity (ϕ_0) and hydrate saturation (S_h). ϕ is defined as the porosity filled only by fluid phases, expressed in Eq. (4)

$$\phi = \phi_0\ (1 - S_h) \tag{4}$$

As porosity is modified, intrinsic permeability k is also updated. T+H uses a permeability reduction factor k_{rF} that is obtained from a power law relationship (Eq. (5)) between the ratios of hydrate-filled porosity ϕ and the hydrate-free porosity ϕ_0. The reduction factor k_{rF} sets the ratio by which intrinsic (hydrate-free) permeability k_0 is decreased, and yields an effective (hydrate-filled) permeability k. The effective permeability k is the permeability of a single-phase fluid flowing in a porous medium with specific saturation of hydrate.

$$\left(\frac{k}{k_0}\right) = k_{rF} = \left(\frac{\phi - \phi_c}{\phi_0 - \phi_c}\right)^m \tag{5}$$

The critical porosity ϕ_c accounts for scenarios of hydrates clogging pore throats and disconnecting fluid-filled pores. It is defined by the product between the saturation of hydrates at which effective permeability is reduced to zero ($maxS_h$), and the hydrate-free porosity (ϕ_0). $\phi_c = \phi_0 \cdot (1 - maxS_h)$.

This approach is similar to the Tokyo model proposed by MASUDA (1997). In both models (Eqs. (5) and (6)), exponents m and N steer the rate by which permeability is reduced. No particular restrictions are given regarding the magnitude of parameters m and N. These fitting parameters accept a wide range of values aimed to make the models fit different scenarios (Fig. 5). Dai and Seol (2014) linked the magnitude of this parameter with pore habits and found that it can vary from N=1.25 for sediments with uniform cementing hydrate, to N=25 for sediments with uniform pore-filling hydrate.

$$\left(\frac{k}{k_0}\right) = (1 - S_h)^N \tag{6}$$

With the small number of measurements used in this study and the fact that all of them are done in the presence of three phases, it was impractical to attempt finding values for parameters m and ϕ_c. Therefore, base values were taken from Birkedal et al. (2014).

Regarding 2-phase flow, T+H keeps the relative permeability model unchanged. However, it uses hydrate saturation (S_h) and the permeability reduction factor (k_{rF}) to obtain the magnitude of effective fluid phase permeability. This involves normalizing the fluid flow saturations

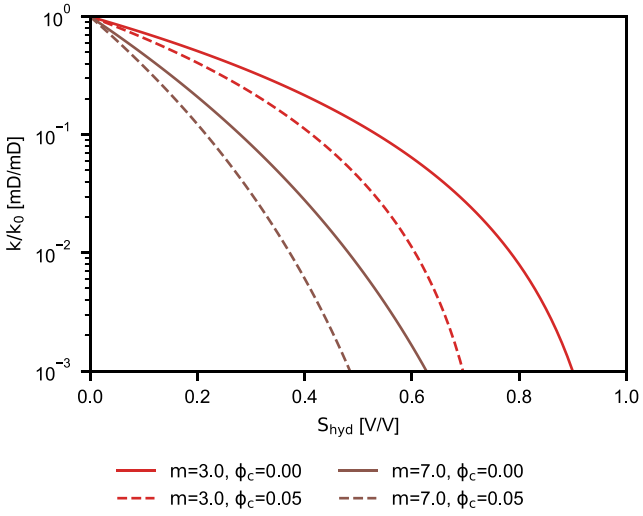

Fig. 5. Hydrate reduction of absolute permeability. Exponent m and critical porosity ϕ_c are fitting parameters. m determines the shape of the curve or the rate at which permeability is reduced. ϕ_c scales the curve on x-axis and sets the point at which permeability is reduced to zero.

(Eqs. (7) and (8)). Solid phases are no longer included as they are an extension of the matrix.

$$S_g^* = \frac{S_g}{(S_g + S_w)} = \frac{S_g}{(1 - S_h)} \tag{7}$$

$$S_w^* = \frac{S_w}{(S_g + S_w)} = \frac{S_w}{(1 - S_h)} \tag{8}$$

These new saturations yield a new relative permeability from Eqs. (3) and (2). To evaluate the effective phase permeability in hydrate bearing systems the relative permeability is 'scaled down' by the permeability reduction factor (Eqs. (9) and (10)).

$$k_w = k_0 \cdot k_{rF}(S_h) \cdot k_{rw}(S_w^*) \tag{9}$$

$$k_g = k_0 \cdot k_{rF}(S_h) \cdot k_{rg}(S_g^*) \tag{10}$$

Capillary pressure was defined by the van Genuchten model (van Genuchten, 1980), with capillary pressure (P_{cap}) as a function of water saturation (S_w), with no hysteresis considered (Fig. 5, Eq. (11)). The remaining terms are fitting parameters set by the user. The only condition is that the magnitude of residual water saturation (S_{irw}) should be smaller than the corresponding parameter in Eqs. (2) and (3). The magnitude of each of these parameters was defined to fit experimental values for capillary entry pressure run on Bentheim sandstone (Raeesi et al., 2014).

$$P_{cap} = -P_0 \left[(S^*)^{1/\lambda} - 1\right]^{1-\lambda} \qquad \text{where } S^* = \frac{S_w - S_{irw}}{S_{mxw} - S_{irw}} \tag{11}$$

As hydrates grow, capillary pressure is scaled with the Leverett model, defined in Eq. (12). Both the hydrate-bearing and hydrate-free porosity and permeability from Eqs. (4) and (5) are used as input. As hydrates are an extension of the matrix, the resulting scaled capillary pressure will reflect a reduction on the effective radii of the pore throats (Fig. 6).

$$P_{cap}^* = P_{cap}\sqrt{\frac{k_0}{k} \cdot \frac{\phi}{\phi_0}} \tag{12}$$

2.1. Model setup

Several numerical simulations in T+H were set to simulate each experiment (Fig. 7). Gridding focused on representing the sandstone

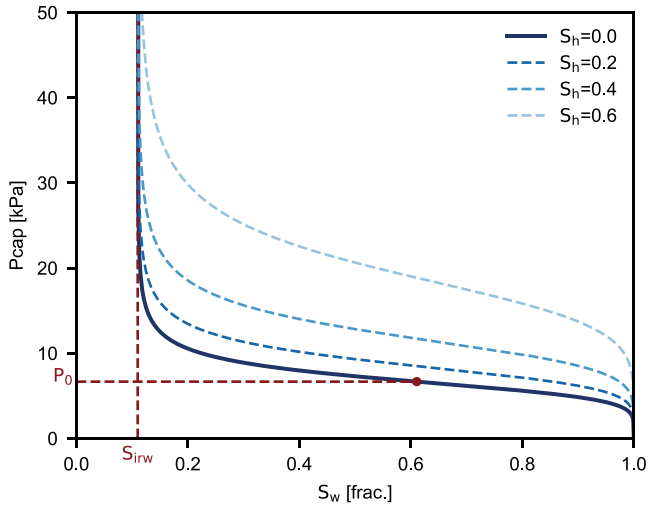

Fig. 6. In dark blue, capillary pressure curve based on van Genuchten model. Parameters P_0 and S_{irw} are highlighted in dark red. In lighter shades of blue, the scaled capillary pressure curves using Leverett model for different hydrate saturation values. (For interpretation of the references to colour in this figure legend, the reader is referred to the web version of this article.)

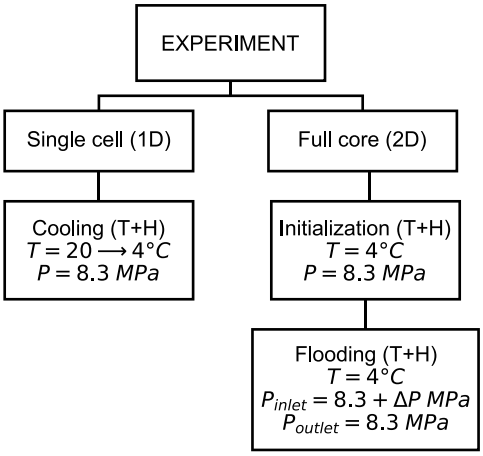

Fig. 7. Overview of simulations set in T+H for each experiment.

core and its interaction with its surroundings with regards to both mass and heat fluxes (Fig. 8).

2.1.1. Single cell simulation

The first set of simulation cases was done on a 1-dimensional representation of the system. This was a material balance exercise to estimate the total saturation of phases and concentration of salinity that an initial mix of brine and methane can yield after cooling down the system. The grid consists of a single element connected to two adjacent boundaries. The cell is initialized with the pre-hydrate fluid saturation values 1 at 20 °C and 8.3 MPa. The adjacent cells are thermodynamic boundaries, set to deliver the heat and mass fluxes necessary to keep the pressure constant and cooling the system down to 4 °C. These simulations were run using the equilibrium model. For comparative purposes, these simulations were reproduced using the kinetic model.

2.1.2. Full core model setup

The horizontal 2-dimensional cartesian grid representation displayed in Fig. 1 was used to simulate core flooding experiments after hydrate formation. Length and width of the full grid are close to the length (14.8 cm) and diameter (5.2 cm) of the core. In comparison to a 3-dimensional model, by reducing the problem by one dimension, the computational cost is minimized without compromising the quality of the results (Birkedal et al., 2014).

Surrounding the grid, boundary conditions were set to emulate the physical elements surrounding core in the experimental setup. To emulate the cooling system, the outer edge of the grid was set to steer and maintain the temperature constant. Permeability and porosity were set to zero, so no mass exchange occurs with the rest of the system.

In between the edge of the grid and the grid representation of the core, grid elements were set to represent the physical elements separating the core from the cooling source such as the steel pieces, the rubber sleeve and the confining fluid. Similarly, permeability and porosity are set to zero to avoid any mass exchange. The main purpose of these grid elements is to steer heat fluxes to emulate the cooling process of the core.

The edges along the y-axis are to represent the flow lines that inject and produce gas. This boundary is also initially set a thermodynamic boundary that actively steer the mass fluxes to sustain pressure.

The main grid is set to represent a Bentheimer sandstone core like the one used in the experiments. Different input parameters are set to describe the physical properties of the medium (Table 2). Similarly, parameters to define relative permeability relationship (Eqs. (3) and (2)) and effect of hydrates in porous media are included (Eq. (5)).

2.1.3. Full core model simulations

The full core grid was used to set up simulations of the core flooding experiments after hydrate formation. For pre-cooling conditions, porous media contain only two fluid phases, methane and brine, and simulation was not needed. Effective permeability was calculated by using the initial saturations of each experiment (Table 1) and Eq. (3).

Initialization at post-cooling conditions. For each experiment, a set of simulations were initialized using the final saturations of gas, brine and hydrate achieved experimentally (Table 1). These simulations were run using the kinetic model.

For initialization of these simulations, distribution of phases was set both homogeneously and heterogeneously. A homogeneous distribution was defined in a way that every single cell of the grid would initialize with the same values of saturation for all three phases. Heterogeneous distributions were set by using a random distribution of values for hydrate saturation. The values of each distribution are truncated between 0 and 1 and their average match the value measured. Multiple variations of standard deviation were set to cover a range of saturation from a narrow (±2 vol.%) to a broad (±50 vol.%) distribution. Fig. 10 shows the resulting distribution of phases for case B, when hydrate saturation has a variance of 36%.

The remaining fluid phases were defined so the bulk saturations of the entire grid would match the experimental values. Capillary effect was considered by setting up simulations with and without capillary pressure scaling. In the simulations without scaling capillary pressure, the fluid phase saturations are set keeping the proportions of the bulk measurements. When capillary pressure scaling is enabled, the distribution of the aqueous phase must be set so the system is in equilibrium in terms of pressure. Eqs. (11) and (12) yield a different capillary pressure (P_{cap}) curve for every value of hydrate saturation. Therefore, for each experiment and grid cell a value of capillary pressure has been determined by solving Eq. (11) for brine saturation (S_w) and that keeps the bulk volumes of all phases equal to the experimental measurements. This yields an accommodation of phases were the remaining pore space in grid cells with a high amount of hydrates is filled mainly by brine and gas fill the cells as hydrate saturation decreases (Figs. 9 and 10).

Flooding. Core flooding simulations were set for both pre- and post-cooling conditions. Pressure at the inlet boundary was set higher than the outlet boundary to induce gas flooding. This pressure difference was set small enough to guarantee that only gas flows in and out of the system and minimal mobilization of brine and phase changes would occur. Effective gas permeability ($k_{g,eff}$) was calculated by Darcy's law

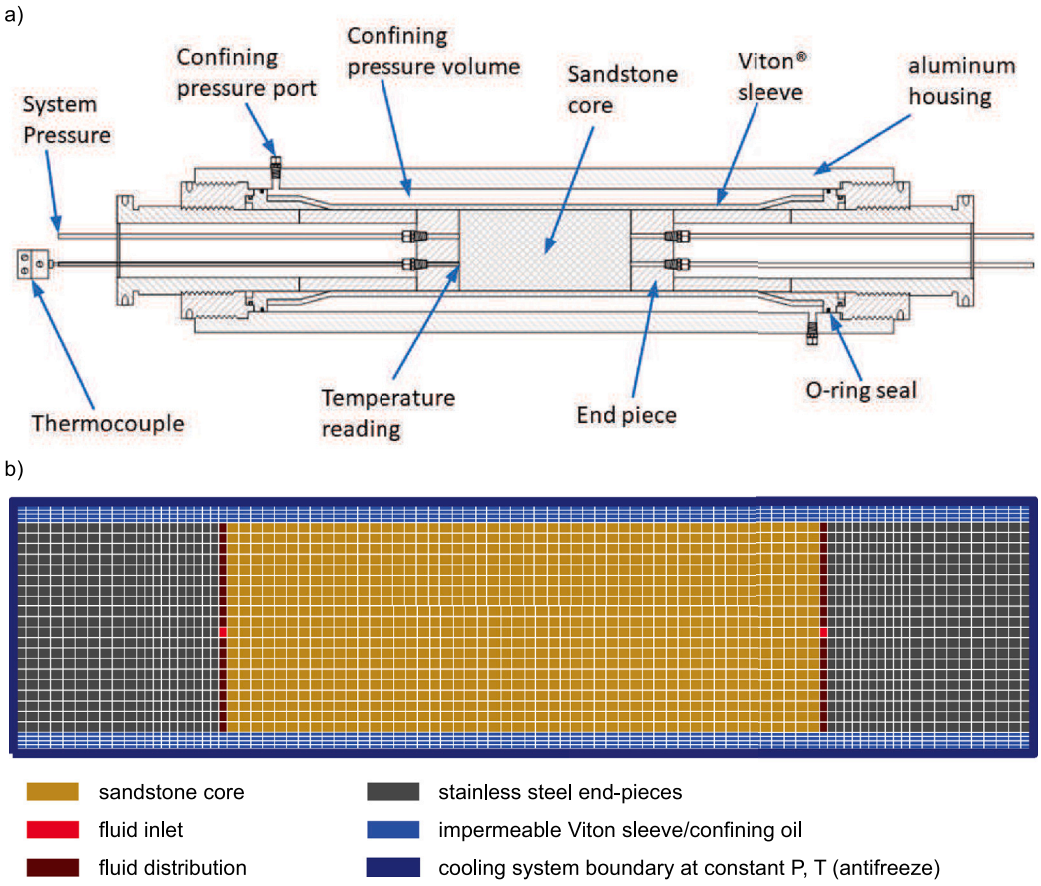

Fig. 8. (a) Cross-sectional view of the composite core holder. Modified from Husebø (2008). (b) Illustration of the numerical system based on the figure above. A no-flow (Neuman) boundary surrounds the system.

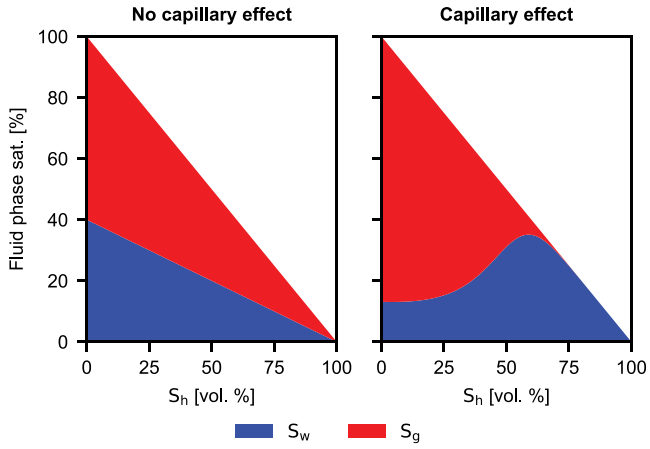

Fig. 9. Schematic representation of how fluid phase saturations are initialized in this study. When no hydrates effect on capillary pressure is considered, fluid phases are defined with the same proportion (left). When hydrates have an effect on capillary pressure (capillary pressure scaling), fluid phases are constrained by the capillary pressure function defined (right). Gas can only invade the larger pores and as hydrate saturation increases, the remaining pore space will be predominantly filled by brine.

defined in Eq. (13). μ_g is viscosity, Δx is the length of the grid in the horizontal axis, Q_g is the volumetric flow across the vertical cross section of the grid, and ΔP is the pressure difference between inlet and outlet of the grid.

$$k_{g,eff} = \mu_g \cdot \frac{\Delta x \cdot Q_g}{\Delta P} \tag{13}$$

3. Results and discussion

3.1. Hydrate formation:1-dimensional model

Simulations using the 1-dimensional model are displayed in Table 3. Hydrate formation yields an increase of salinity from 3.5 to 14 wt% NaCl, which matches the inhibition level of methane hydrate with NaCl at 8.3 MPa and 4 °C, confirming that the system has reached equilibrium. Fig. 11 shows the comparison between these simulations and the laboratory experiments.

In general, all simulations yielded equal or more hydrates than the experiments. All phase saturations showed variations in comparison to the experimental results. Largest variations are observed in final brine and hydrate saturation. Experiment A was initialized with the highest gas saturation (54 vol. %). Its simulation matched experimental results within the range of uncertainty.

Experiments B, C, D and E were initialized with a gas saturation between 46 and 47 vol. %. However, they all yielded different amounts of hydrates (45–51 vol. %) reflecting a limitation on the repeatability of results. Numerically, these simulations yielded more hydrates than any of the experiments (53 vol.%).

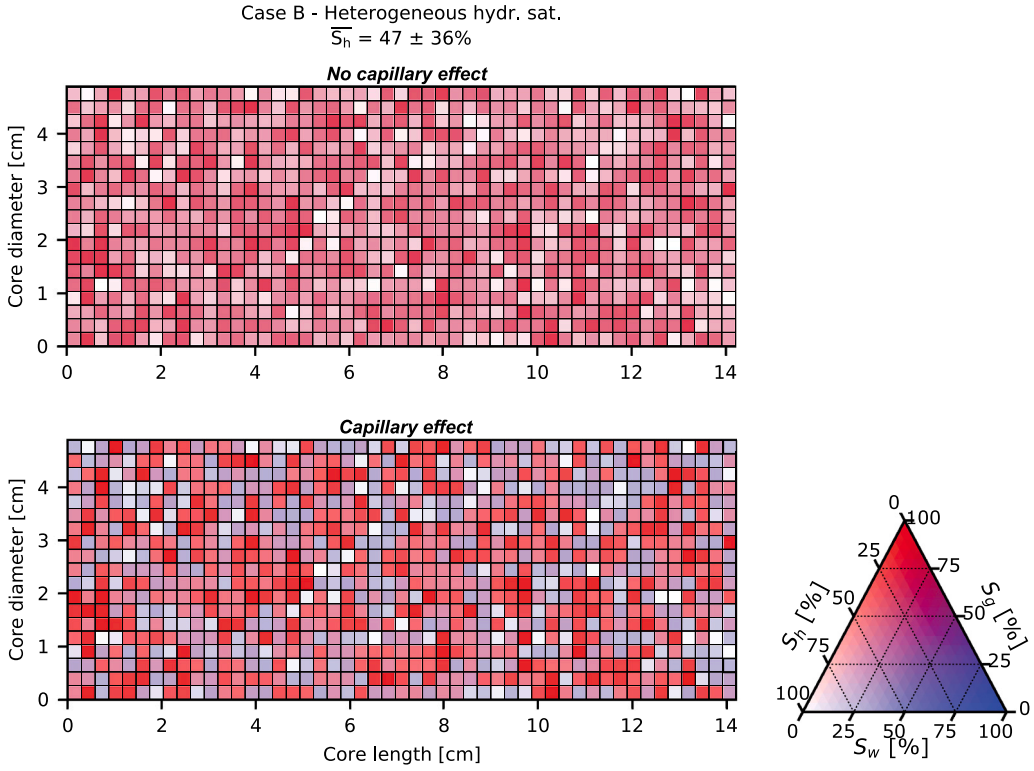

Fig. 10. Heterogeneous distribution of phases set for case B. The bulk phase saturations are equal to those obtained experimentally ($S_h = 47\%$, $S_g = 36\%$, $S_w = 17\%$). At a grid cell level, the magnitude for hydrate saturation is set randomly using a normal distribution defined by the measured hydrate saturation as its mean (47%), and a variance of ±36%. When no hydrate present does not affect capillary pressure (top figure), the non-hydrate filled pore space is set proportionally to the measurements of gas an brine saturation ($S_g = 36\%$, $S_w = 17\%$). To account for the effect of hydrates on capillary pressure (bottom figure), fluid phases are redistributed to achieve equilibrium.

Table 3
Comparison between saturation and salinity before and after cooling from single cell (1-dimensional) simulation for each experiment. S_w, S_g and S_h are volume fraction saturations for brine, gas and hydrate respectively. X_{inh} is salinity concentration.

Exp. ID	Input (T=20 °C)			Output (T=4 °C)			
	S_w	S_g	X_{inh}	S_w	S_g	S_h	X_{inh}
A	4.60E−01	5.40E−01	3.50E−02	9.88E−02	4.47E−01	4.54E−01	1.40E−01
B	5.30E−01	4.70E−01	3.50E−02	1.14E−01	3.63E−01	5.23E−01	1.40E−01
C	5.40E−01	4.60E−01	3.50E−02	1.16E−01	3.51E−01	5.33E−01	1.40E−01
D	5.40E−01	4.60E−01	3.50E−02	1.16E−01	3.51E−01	5.33E−01	1.40E−01
E	5.40E−01	4.60E−01	3.50E−02	1.16E−01	3.51E−01	5.33E−01	1.40E−01
F	6.40E−01	3.60E−01	3.50E−02	1.37E−01	2.31E−01	6.32E−01	1.40E−01
G	6.40E−01	3.60E−01	3.50E−02	1.37E−01	2.31E−01	6.32E−01	1.40E−01
H	7.30E−01	2.70E−01	3.50E−02	1.57E−01	1.23E−01	7.20E−01	1.40E−01

This pattern was repeated in experiments F and G. Both experiments were initialized with less gas than previous experiments (36 vol.%). The amount of hydrates formed was not reproduced experimentally either (53–61 vol.%), and such amount was less than the one formed numerically (63 vol.%).

Finally, experiment H was initialized with the lowest gas saturation (27 vol.%). The discrepancies between simulations and experiments were higher in this case. Simulation of this experiment yielded almost twice the hydrates formed experimentally and a third of the brine. Simulated final gas saturation was also a fraction of the experimental measurement.

In experiments B to H, as more hydrates are formed, the final brine saturation decreased correspondingly. Gas saturation remained similar in all experiments but experiment H, where final gas saturation is close to two thirds of the value obtained in the lab.

Whereas the experiments are constrained by both equilibrium and kinetics, the single cell simulations are in equilibrium and are only constrained by pressure, temperature and initial fluid in place. They return a material balance with no regard of the porous medium properties, where both cooling and hydrate formation occur homogeneously. These results can be regarded as the potential maximum amount of hydrates a given distribution of gas and brine can yield. The discrepancy between these and the experimental measurements suggests that experiments are not being able to form as much hydrates as they could potentially form.

Experimentally, gas must move throughout the core, limited by the intrinsic permeability of the porous medium and its initial saturation. As hydrates start forming, these are not formed homogeneously. At the pore scale, nucleation of hydrate will occur if both gas and brine are present. However, as hydrates form these will consume both phases and will need supply of either to form more hydrates. The rate at which more gas arrives will be limited by the reduced gas saturation. If all gas is consumed in a region of the core, such region is left with only hydrate and brine. In order to have more gas invading this sector, this stream of gas has to overcome the capillary entry pressure. In addition, the random nature of hydrate nucleation most likely creates stochastic flow barriers that progressively limit the flow. So, a low amount of hydrates returned by experiments, could be caused by gas not being

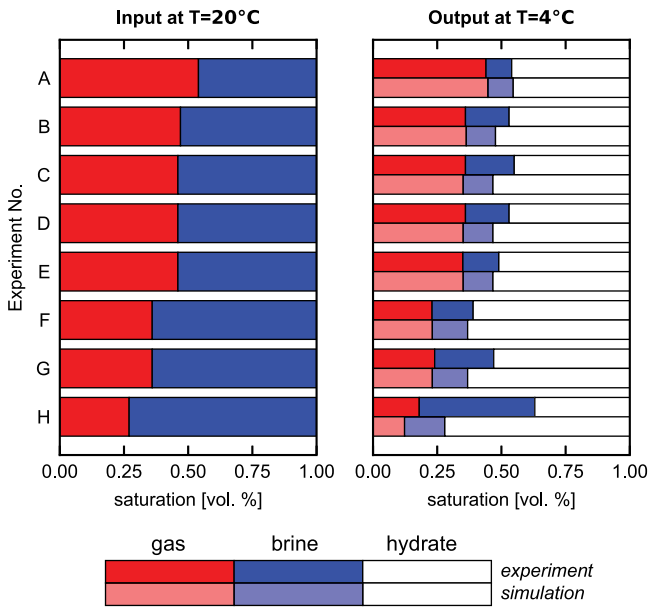

Fig. 11. Overview of phase saturations measured before and after cooling down. In a lighter shade of colour, modelled saturations from single cell simulations are added for comparison. (For interpretation of the references to colour in this figure legend, the reader is referred to the web version of this article.)

able to reach inner parts of the core due to hydrates limiting flow. They can also be caused by portions of the core saturated with either gas or brine with few contact points.

This is reflected in the fact that simulations yielded more hydrates in all cases but experiment A. Experiment A has the highest initial saturation of gas (S_{g0}) which means the initial effective permeability of gas (k_{g0}) is higher than any other experiment, allowing more gas to flow in the core as hydrates form. In contrast, experiment H has the lowest S_{g0} and its simulation returned the largest discrepancy in hydrate saturation (S_h). This means, although there is an excess of brine, it can only form hydrates with the gas that is in contact with brine. By the time hydrates start growing, gas supply is limited to reach remaining brine.

3.2. Hydrate effects on gas permeability

For the full core model simulations, methane relative permeability estimations were produced for cases with both a homogeneous and a heterogeneous distribution of fluid and solid phases. Simulations using a homogeneous distribution of phases, always returned a relative permeability higher than experiments (Table 4). Setting exponent m in Eq. (5) as 3, experiment A produced a value about 6 times higher than the measured value. This difference becomes higher in the remaining experiments, modelled values may be four orders of magnitude higher than the experimental values.

When m of Eq. (5) is increased to 5.4, methane permeability decreases but the modelled results are still higher than experimental ones (Table 4). Modelled methane relative permeability for experiment A has a magnitude close to the measured value. However, remaining experiments show a variation of modelled values up to 3 orders of magnitude higher than the measured ones.

As control points, relative permeability was also estimated by using the input phase saturations and the models defining equations (Eqs. (5) and (10)). The small change discrepancy between both values (Table 4 columns *from EQ* and *simulated*) respond to small changes in hydrate saturation during flooding, but still not high enough to change the bulk saturation of the grid.

These simulations show that the permeability reduction model (Eq. (5)) is not able to provide a unique solution that matches the experimental results. This suggests that reductions in gas relative permeability k_{rg} may not be caused exclusively by the permeability reduction factor K_{rF}.

By being a function of hydrate saturation (S_h), this model (Eq. (5)) does not account for changes in pore geometry caused by hydrate formation. Though the model is flexible to set the decrease of permeability to fit different pore habits (Dai and Seol, 2014), it does not consider the occurrence of multiple pore habits in a single lithology or the shifting between different habits with the change of hydrate saturation (Teng and Zhang, 2020). Dai and Seol (2014) have pointed out that in these types of models, the determination of fitting parameters like N or m lack a sound physical foundation and cannot be estimated based on lithology or other remotely detectable reservoir parameters.

These observations and the unlikelihood of having a homogeneous distribution of both fluid and hydrate justify testing a stochastic distribution of hydrates, closer to the "patchy" pattern that has been observed in hydrate-bearing sediments (Fig. 1).

A heterogeneous distribution of solid phases causes a reduction of the effective gas permeability. When the hydrate effect on capillary pressure is not considered (Fig. 12 left), permeability gets progressively smaller as the distribution of hydrates is more heterogeneous. With the broadest distribution permeability decreased by near one order of magnitude in all experiments. However, in this scenario, fluid phase saturations are proportional to the bulk saturations of the core (Fig. 9 left).

When the hydrate effect on capillary pressure is considered (12 right), the change from homogeneous to heterogeneous is more pronounced than in the previous simulations. This decline ranged from 1 order of magnitude lower in experiment A to almost 3 orders of magnitude in experiment H. The main reason for such decrease is that the capillary entry pressure in each cell has been scaled up by the hydrate saturation (Eq. (12)). Higher capillary pressure results in gas being accommodated preferentially to the cells with lower hydrate saturation. On the other end, cells with higher hydrate saturation will have the remaining pore space filled mainly by brine (Fig. 12 left). Injected gas is then able to move through those cells with low hydrate saturation. In contrast, its flow will be limited in the remaining cells by both hydrate and the low saturation of gas.

The set of simulations that considers the effect of hydrates on both capillary pressure and permeability yields results closer to those obtained experimentally (see Fig. 12). However, there is still a gap between modelled and measured values of methane relative permeability. Modelled results for experiment A yielded a close match for the two broadest distributions ($\sigma = \pm 36$ vol.%, ± 50 vol.%). To a lesser degree, a similar situation was observed in experiment B. However, remaining simulations returned values between one and two orders of magnitude higher than laboratory measurements (see Fig. 13).

The results suggest that the impact of a random pattern of hydrate growth on effective fluid flow cause reductions of relative permeability close to those observed in the laboratory. The same mechanism may also explain the limitations that can constrain the flow of gas and limit the amount of hydrates formed during cooling.

However, there are still gaps to achieve a better match between simulations and experiments. Such gaps are not necessarily explained only by the uncertainty of the input to the models, but can be caused by processes, that are not represented by the model.

Variations on experiments results that were initialized with similar phase saturations (B, C, D, E and F, G) suggest that the resulting distribution of hydrates may not be only heterogeneous but may follow a preferential pattern constrained by the rate at which the system was cooled down internally. A scenario where initial nucleation is located towards the outer rim of the core is possible. In this situation the edges of the core will meet the conditions to form hydrate first, and therefore limit the flow of gas towards the inner part of the core. This yields a

Table 4
Comparison between methane measured and modelled methane relative permeability Modelled values include preliminary calculations using Eq. (10) and simulated obtained from Darcy's law using simulated volumetric flow and differential pressure. These values include output for two different exponents m for Eq. (5).

Exp. ID	S_h	S_g	k_{rg} [frac.]				
	[frac.]	[frac.]	Measured	Modelled			
	±0.02	±0.02		m=3.0, ϕ_c=0.05		m=5.44, ϕ_c=0.05	
				From EQ.	Simulated	From EQ.	Simulated
A	0.46	0.44	1.9E−2 ± 0.3E−2	1.11E−01	1.17E−01	2.20E−02	2.28E−02
B	0.47	0.36	1.2E−3 ± 0.4E−3	5.72E−02	6.00E−02	1.08E−02	1.13E−02
C	0.45	0.36	1.7E−6 ± 0.6E−6	5.72E−02	5.60E−02	1.19E−02	1.17E−02
D	0.47	0.36	4.0E−6 ± 1.0E−6	5.72E−02	5.61E−02	1.08E−02	1.06E−02
E	0.51	0.35	1.4E−4 ± 0.5E−4	5.20E−02	5.12E−02	7.95E−03	7.75E−03
F	0.61	0.23	4.0E−7 ± 1.0E−7	1.27E−02	1.33E−02	1.04E−03	1.08E−03
G	0.53	0.24	9.9E−7 ± 0.8E−7	1.49E−02	1.54E−02	2.03E−03	2.11E−03
H	0.37	0.18	7.1E−7 ± 0.8E−7	5.51E−03	5.60E−03	1.65E−03	1.70E−03

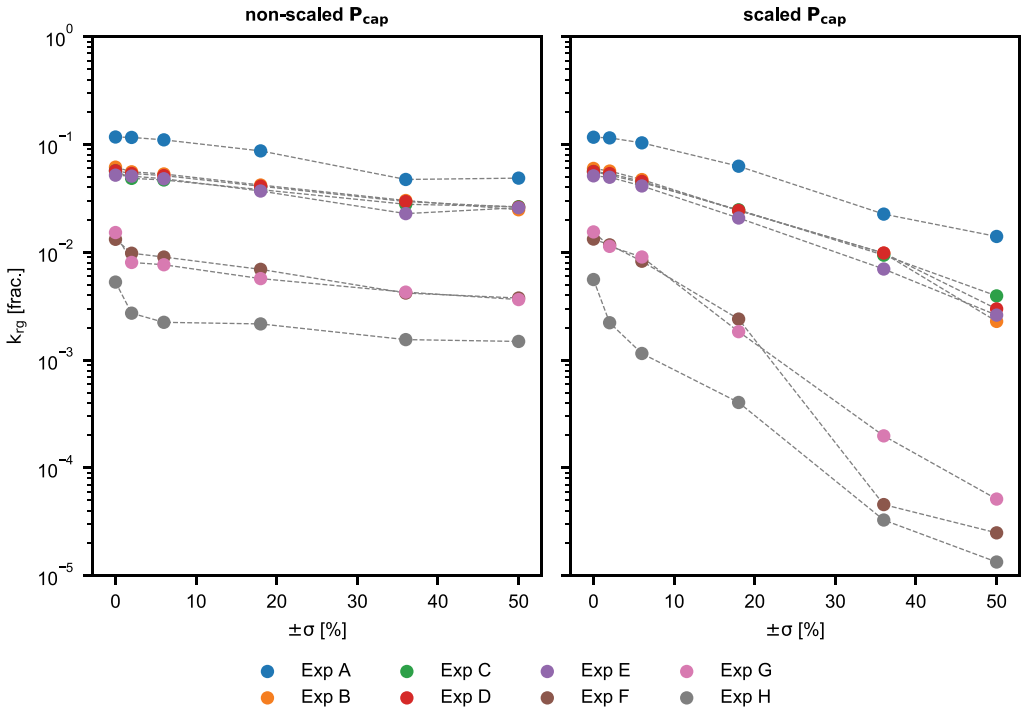

Fig. 12. Simulated methane relative permeability versus std deviation of hydrate distribution for simulations considering only hydrate effects on permeability (left) and for simulations considering hydrate effects on both permeability and capillary pressure. For each experiment, the average phase saturation remains constant, but its standard deviation changes from 0 to 50%.

limited amount of gas to form hydrates towards the middle of the core, and an effective reduction of permeability along the long axis of the core.

The saturation heterogeneities formed during hydrate growth are probably caused by local consumption of gas and water, as well as local reduction of porosity. These processes will cause driving forces to change rapidly. However, the effects may disappear or be enhanced over the natural timescales. For instance, unless replenished by gas, hydrates will eventually dissolve and disappear. One may also imagine processes as Ostwald ripening driving changes in the heterogeneities, perhaps enhancing the appearance of veins and patches.

These observations reflect the challenges of measuring relative gas permeability in hydrate bearing sediments. Though it is possible to perform a core flooding procedure with success, the resulting flow of gas will be constrained by the internal distribution of hydrates inside the core. In addition, the development of capillary barriers will decrease the flow of gas. Finally, if hydrates are being formed preferentially in the outer parts of the core, a low saturation of hydrates concentrated in this part can be enough to further the reduction of effective fluid flow.

4. Conclusions

- Experimental characterization and subsequent model implementation of the heterogeneities is necessary in order to model hydrate permeabilities. The impact that the heterogeneous nature of hydrate formation on sediment has on flow is seen in this study.
- Consistency testing by initial 1D modelling is valuable for comparing experimental and calculated bulk saturations. Discrepancies may indicate hydrate driven flow barriers.
- Adding heterogeneities to the hydrate saturation as seen in MRI experiments, are necessary in order to simulate the experimental trend of the permeabilities.
- Application of a capillary entry pressure is necessary to model regions where all the gas been consumed.

CRediT authorship contribution statement

Alejandro Bello-Palacios: Conceptualization, Methodology, Software, Formal analysis, Writing – original draft. **Per Fotland:** Supervision, Writing – review & editing. **Stian Almenningen:** Resources,

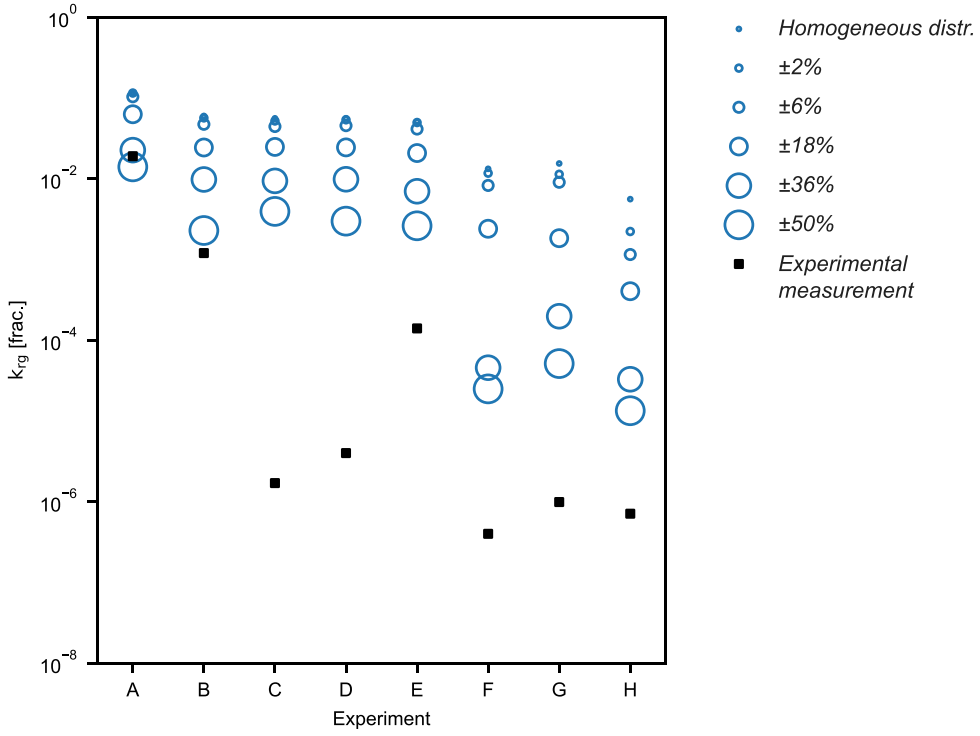

Fig. 13. Comparison between measurements of methane relative permeability (black squares) and simulated estimations (blue circles). The radius of the circles represents the standard deviation of the phase saturations within the grid. Smallest circles correspond to homogeneous distribution and the largest circle to a distribution with a broad variation ($\sigma = \pm 50\%$).

Writing – review & editing. **Geir Ersland:** Supervision, Writing – review & editing.

Declaration of competing interest

The authors declare that they have no known competing financial interests or personal relationships that could have appeared to influence the work reported in this paper.

Acknowledgements

This work was supported by funding from the Norwegian Research Council. Equinor ASA is thanked for permission to publish this work.

References

Ahn, T., Lee, J., Huh, D.G., Kang, J.M., 2005. Experimental study on two-phase flow in artificial hydrate-bearing sediments. Geosyst. Eng. 8, 101–104. http://dx.doi.org/10.1080/12269328.2005.10541244.

Almenningen, S., Gauteplass, J., Hauge, L.P., Barth, T., Fernø, M.A., Ersland, G., 2019. Measurements of ch_4 and co_2 relative permeability in hydrate-bearing sandstone. J. Pet. Sci. Eng. 177, 880–888. http://dx.doi.org/10.1016/j.petrol.2019.02.091.

Birkedal, K.A., Freeman, C.M., Moridis, G.J., Graue, A., 2014. Numerical predictions of experimentally observed methane hydrate dissociation and reformation in sandstone. Energy Fuels 28, 5573–5586. http://dx.doi.org/10.1021/ef500255y.

Boswell, R., 2009. Engineering. is gas hydrate energy within reach? Science 325, 957–958. http://dx.doi.org/10.1126/science.1175074, URL: https://www.ncbi.nlm.nih.gov/pubmed/19696340.

Chen, X., Verma, R., Espinoza, D.N., Prodanović, M., 2018. Pore-scale determination of gas relative permeability in hydrate-bearing sediments using x-ray computed micro-tomography and lattice boltzmann method. Water Resour. Res. 54, 600–608. http://dx.doi.org/10.1002/2017wr021851.

Collett, T., Bahk, J.J., Baker, R., Boswell, R., Divins, D., Frye, M., Goldberg, D., Husebø, J., Koh, C., Malone, M., Morell, M., Myers, G., Shipp, C., Torres, M., 2014. Methane hydrates in nature—current knowledge and challenges. J. Chem. Eng. Data 60, 319–329. http://dx.doi.org/10.1021/je500604h.

Dai, S., Seol, Y., 2014. Water permeability in hydrate-bearing sediments: A pore-scale study. Geophys. Res. Lett. 41, 4176–4184. http://dx.doi.org/10.1002/2014GL060535, URL: https://agupubs.onlinelibrary.wiley.com/doi/abs/10.1002/2014GL060535. arXiv:https://agupubs.onlinelibrary.wiley.com/doi/pdf/10.1002/2014GL060535.

Husebø, J., 2008. Monitoring Depressurization and CO_2-CH_4 Exchange Production Scenarios for Natural Gas Hydrates (Ph.D. thesis). University of Bergen.

Jaiswal, N.J., 2004. Measurement of Gas-Water Relative Permeabilities in Hydrate Systems (Ph.D. thesis). University of Alaska Fairbanks.

Jang, J., Santamarina, J.C., 2014. Evolution of gas saturation and relative permeability during gas production from hydrate-bearing sediments: Gas invasion vs. gas nucleation. J. Geophys. Res.: Solid Earth 119, 116–126. http://dx.doi.org/10.1002/2013jb010480.

Jang, J., Santamarina, J.C., 2016. Hydrate bearing clayey sediments: Formation and gas production concepts. Mar. Pet. Geol. 77, 235–246. http://dx.doi.org/10.1016/j.marpetgeo.2016.06.013.

Johnson, A., Patil, S., Dandekar, A., 2011. Experimental investigation of gas-water relative permeability for gas-hydrate-bearing sediments from the mount elbert gas hydrate stratigraphic test well, alaska north slope. Mar. Pet. Geol. 28, 419–426. http://dx.doi.org/10.1016/j.marpetgeo.2009.10.013.

Kim, H.C., Bishnoi, P.R., Heidemann, R.A., Rizvi, S.S.H., 1987. Kinetics of methane hydrate decomposition. Chem. Eng. Sci. 42, 1645–1653. http://dx.doi.org/10.1016/0009-2509(87)80169-0.

Kleinberg, R.L., Flaum, C., Griffin, D.D., Brewer, P.G., Malby, G.E., Peltzer, E.T., Yesinowski, J.P., 2003. Deep sea nmr: Methane hydrate growth habit in porous media and its relationship to hydraulic permeability, deposit accumulation, and submarine slope stability. J. Geophys. Res.: Solid Earth 108, http://dx.doi.org/10.1029/2003jb002389.

Kowalsky, M.B., Moridis, G.J., 2007. Comparison of kinetic and equilibrium reaction models in simulating gas hydrate behavior in porous media. Energy Convers. Manage. 48, 1850–1863. http://dx.doi.org/10.1016/j.enconman.2007.01.017.

Li, G., Li, C., Li, X., Wei, N., 2018. Permeability experiments on the methane hydrate in quartz sands and its model verification. Nat. Gas Ind. B 5, 298–305. http://dx.doi.org/10.1016/j.ngib.2017.12.009.

MASUDA, Y., 1997. Numerical calculation of gas production performance from reservoirs containing natural gas hydrates. In: Annual Technical Conference. Soc. of Petrol. Eng., San Antonio, Tex., URL: https://ci.nii.ac.jp/naid/10025408647/en/.

Moridis, G.J., Collett, T.S., Pooladi-Darvish, M., Hancock, S., Santamarina, C., Boswell, R., Kneafsey, T., Rutqvist, J., Kowalsky, M., Reagan, M.T., Sloan, E.D., Sum, A.K., Koh, C., 2010. Challenges, uncertainties and issues facing gas production from gas hydrate deposits. SPE Reserv. Eval. Eng. Medium: ED. URL: https://www.osti.gov/servlets/purl/1005168.

Moridis, G., Pruess, K., 2014. User's Manual of the Tough+ V1. 5 Core Code: A General Purpose Simulator of Non-Isothermal Flow and Transport Through Porous and Fractured Media. Report, Lawrence Berkeley National Laboratory, URL: http://tough.lbl.gov/assets/files/02/documentation/TH_Manual_v1.5s.pdf.

Raeesi, B., Morrow, N.R., Mason, G., 2014. Capillary pressure hysteresis behavior of three sandstones measured with a multistep outflow-inflow apparatus. Vadose Zone J. 13, http://dx.doi.org/10.2136/vzj2013.06.0097.

Ren, X., Guo, Z., Ning, F., Ma, S., 2020. Permeability of hydrate-bearing sediments. Earth-Sci. Rev. 202, http://dx.doi.org/10.1016/j.earscirev.2020.103100.

Sloan, E., Dendy, J., Koh, C., 2007. Clathrate Hydrates of Natural Gases. CRC Press LLC, Bosa Roca, United States.

Teng, Y., Zhang, D., 2020. Comprehensive study and comparison of equilibrium and kinetic models in simulation of hydrate reaction in porous media. J. Comput. Phys. 404, 109094. http://dx.doi.org/10.1016/j.jcp.2019.109094, URL: https://www.sciencedirect.com/science/article/pii/S0021999119307995.

van Genuchten, M.T., 1980. A closed-form equation for predicting the hydraulic conductivity of unsaturated soils. Soil Sci. Am. J. 44, 892–898. http://dx.doi.org/10.2136/sssaj1980.03615995004400050002x.